MTLA 43 (2025) 102512

Contents lists available at ScienceDirect

Materialia

journal homepage: www.elsevier.com/locate/mtla

Full Length Article

Microstructural evolution and phase stability in Nb-containing interstitial Fe-Mn-Co-Cr-C high-entropy alloys: An in-situ synchrotron X-ray diffraction study during laser melting

I.A.B. Moura [a,b,*], G.G. Ribamar [c,d], A.C. Chuang [e], T.S. Nunes [f], Jiajia Shen [c], Wei Zhang [g], P. Freitas Rodrigues [b], A.B. Pereira [d], Yutao Pei [g], F. Zhang [h], J.P. Oliveira [c,*]

[a] UNIDEMI, Department of Mechanical Engineering, NOVA School of Science and Technology, Universidade NOVA de Lisboa, Caparica 2829-516, Portugal
[b] CEMMPRE, ARISE, Department of Mechanical Engineering, University of Coimbra, Coimbra 3030-788, Portugal
[c] CENIMAT/I3N, Department of Materials Science, NOVA School of Science and Technology, Universidade NOVA de Lisboa, Caparica, 2829-516, Portugal
[d] Department of Mechanical Engineering, Campus de Santiago, TEMA—Centre for Mechanical Technology and Automation, University of Aveiro, Aveiro 3810-193, Portugal
[e] X-ray Science Division, Advanced Photon Source, Argonne National Laboratory, Lemont, IL 60439, USA
[f] Department of Materials Science, Military Institute of Engineering - IME, Praça General Tibúrcio 80, Rio de Janeiro, RJ 22290-270, Brazil
[g] Advanced Production Engineering, Faculty of Science and Engineering, Engineering and Technology Institute Groningen, University of Groningen, Nijenborgh 4, AG 9747, the Netherlands
[h] Materials Measurement Science Division, National Institute of Standards and Technology, 100 Bureau Drive, Gaithersburg, MD 20899, USA

ARTICLE INFO

Keywords:
Synchrotron radiation
Multicomponent solidification
Rapid solidification
Solidification microstructure
Interstitial high entropy alloys

ABSTRACT

The influence of Nb on phase stability and microstructural evolution in an interstitial Fe-Mn-Co-Cr-C high-entropy alloy was investigated using in-situ synchrotron X-ray diffraction (SXRD) during laser melting. Scheil-Gulliver simulations predict the formation of σ and γ-f.c.c. phases in all three alloys, along with NbC in Nb-containing compositions. SXRD confirmed the presence of most predicted phases, but the σ phase was absent. Nb promotes crystallite refinement and increases dislocation density, though excessive additions reduce refinement efficiency due to solubility limits and secondary phase formation. Furthermore, Nb addition also enhances ε-h.c.p. phase formation by reducing stacking fault energy through NbC-induced carbon depletion. Analysis of intensity peak evolution reveals that Nb alters preferred grain orientations, reducing $\{111\}_\gamma$ intensity while enhancing $\{220\}_\gamma$, leading to a more isotropic grain distribution. Overall, Nb plays a key role in phase selection, microstructure refinement, and preferred orientation evolution, allowing the tailored microstructure of high-entropy alloys via rapid solidification.

1. Introduction

The development of high-entropy alloys (HEAs), defined by their multi-principal element compositions, has revolutionized alloy design by enabling unprecedented access to vast compositional spaces beyond traditional metallurgy [1–3]. These materials exhibit exceptional mechanical performance, thermal stability, and corrosion resistance, arising from core effects such as severe lattice distortion, sluggish diffusion, and high configurational entropy [4–6]. More recently, interstitial high-entropy alloys (iHEAs) have emerged as a promising subclass, wherein the incorporation of small interstitial atoms (e.g., C, N, B) into HEAs leads to enhanced strength-ductility synergy through mechanisms including interstitial solid solution hardening, lattice strain amplification, and dislocation–interstitial interactions [7–9]. Recent studies on FeMnCoCrC iHEAs have demonstrated remarkable mechanical properties due to their hierarchical microstructures and complex deformation modes [10–13]. These iHEAs typically exhibit a face-centered cubic (FCC) matrix, which may partially transform into ε-martensite under deformation. This transformation induces a transformation-induced plasticity (TRIP) effect, enhancing both strength and ductility [13,14]. In parallel, niobium (Nb) addition has been explored as a route to tune microstructure in various HEAs, such as CoCrFeNi [15], CoFeNiVMo [16], CoCrCuFeNi [17], and AlCrFeCoNi [18], by promoting grain refinement, lattice distortion, and carbide

* Corresponding authors.
E-mail addresses: ia.moura@campus.fct.unl.pt (I.A.B. Moura), jp.oliveira@fct.unl.pt (J.P. Oliveira).

https://doi.org/10.1016/j.mtla.2025.102512
Received 26 June 2025; Accepted 1 August 2025
Available online 4 August 2025

precipitation, all of which contribute to strengthening and phase stabilization.

Laser melting is widely utilized in welding and additive manufacturing (AM) of metal parts due to its high precision and rapid energy input [19]. These techniques enable precise fabrication of complex geometries and promote non-equilibrium phase formation and fine microstructural refinement, making them particularly attractive for the development of advanced HEAs [14,20,21]. Despite these advantages, the role of Nb in iHEAs processed via AM remains underexplored, especially in terms of its influence on phase stability, carbide precipitation, and defect evolution under high solidification rates. the incorporation of Nb in iHEAs produced via AM remains relatively underexplored. Nonetheless, recent studies have begun to shed light on this topic. For instance, Zhang et al. [20] demonstrated that Nb addition in laser powder bed fusion (LPBF) processed CoCrFeMnNi HEAs induces significant grain refinement and modified precipitation behavior. Pegues et al. [21] further reported that increasing Nb content in laser-beam directed energy deposition (LB-DED) fabricated CoCrFeMnNi HEAs led to the formation of a multiphase structure with enhanced hardness, attributed to the emergence of hexagonal close-packed (hcp) phases. In a related study, Zhang et al. [14] employed laser metal deposition (LMD) to synthesize a Nb-containing FeMnCoCrC iHEAs, achieving improved tensile strength while preserving ductility, an outcome ascribed to the combined effects of lattice distortion, increased dislocation density, and carbide precipitation.

While these studies have elucidated the benefits of Nb alloying in various HEA systems, its specific role in promoting NbC precipitation and modulating phase stability under rapid solidification conditions – such as those experienced during AM – remains less well understood. Although thermodynamic modeling predicts NbC formation in the presence of C microalloying [22], the isolated effects of Nb addition, particularly in carbon-containing iHEAs, have not been systematically investigated. This knowledge gap is especially pertinent given that laser processing imposes extreme thermal gradients and high cooling rates, which significantly influence solidification pathways, defect structures, and phase transformation kinetics.

To address this gap, the present study investigates the phase evolution behavior of Nb-containing interstitial HEAs subjected to rapid solidification via single-pass laser melting. While this approach does not fully replicate the complexity of layer-by-layer AM, it offers a highly controlled and reproducible platform to study fundamental microstructural responses to localized laser heating. In situ high-energy synchrotron X-ray diffraction (SXRD) was employed to monitor the real-time evolution of crystalline phases during laser melting and cooling. This time-resolved approach enables direct correlation between laser-induced thermal history and phase transformation mechanisms, thereby providing novel insights into the role of Nb in influencing solidification dynamics, phase stability, and potential carbide formation in iHEAs. These findings contribute to a deeper mechanistic understanding essential for guiding future alloy design and process optimization in AM of advanced Nb-containing iHEA systems.

2. Materials and methods

2.1. Experimental materials and laser processing

Pre-alloyed iHEA powders with compositions of $Fe_{49.5}Mn_{30}Co_{10}Cr_{10}C_{0.5}$ (%, atomic fraction) and Nb-containing variants (0.5 wt. % and 1.0 wt. % Nb) were produced by gas atomization and supplied by ANHUI FITECH MATERIALS CO., LTD. The average atomic masses of the alloys were calculated based on their nominal compositions as 55.28 $g{\cdot}mol^{-1}$ for the base alloy, increasing to 55.39 $g{\cdot}mol^{-1}$ and 55.50 $g{\cdot}mol^{-1}$ for the 0.5 wt. % and 1.0 wt. % Nb-containing alloys, respectively. Niobium was incorporated directly into the melt before atomization, resulting in chemically homogeneous pre-alloyed powders, with no post-synthesis mixing required. The particle size distribution of all powders ranged from 15 to 53 μm. No additional blending or mechanical alloying was performed. All powders were used as received for subsequent processing and characterization.

The pre-alloyed powders were processed using LPBF on an SLM125 HL system[1] under an argon atmosphere to fabricate dense plates. The LPBF processing parameters were set to a laser power of 300 W, a scanning speed of 700 mm/s, a hatch spacing of 120 μm, a layer thickness of 30 μm, and a 67° rotation between layers. These LPBF-fabricated plates were subsequently used in SXRD in situ laser melting experiments. The laser melting parameters and sample nomenclature are summarized in Table 1.

2.2. In-situ synchrotron X-ray diffraction (SXRD) setup

In-situ laser-melting SXRD experiments were conducted at beamline 1-ID-E of the Advanced Photon Source (APS), Argonne National Laboratory, to elucidate the phase evolution dynamics during the material production. The experimental setup, detailed by Oh et al. [19] and depicted in Fig. 1, involved a continuous-wave single-mode ytterbium fiber laser (model YLR-500-AC, IPG Photonics) guided by a galvo scanner (IntelliSCANde 30, SCANLAB GmbH) for precise laser scanning. A stationary micro-focused high-energy X-ray beam source of 50 × 35 μm, with an energy of 61.3 keV (λ = 0.202 Å) was directed through the samples within an argon-filled chamber. Debye-Scherrer diffraction cones, generated by the interaction of the X-ray beam with the samples, were recorded as diffraction rings on a detector PILATUS 3X-2 M DECTRIS at a frame rate of 250 Hz (1 image every 4 ms) with a 1 ms exposure time per frame.

2.3. Diffraction data processing and phase quantification

The raw 2D Debye-Scherrer diffraction images were converted into 1D diffraction patterns using full integration over the azimuthal angle via the open-source software Pydidas [23] providing a comprehensive overview of microstructural evolution during cooling. Peak fitting analysis within Pydidas enabled precise determination of peak positions, integrated intensities, and full width at half-maximum (FWHM) information for each lattice family plane. The phase volume fractions were quantified according to the methodology found in [24–26]. In-house Python routines were then employed for calculations and data visualization.

3. Results and discussion

3.1. Thermodynamic simulation and phase identification

Fig. 2 depicts the Scheil-Gulliver solidification curves, calculated using ThermoCalc software with the TCHEA5.2 HEA database, alongside

Table 1
Laser melting parameters used for the iHEAs.

Sample	Laser power (P, W)	Scan speed (V, mm/s)	Laser beam size (μm)
iHEA	500	400	150
iHEA-0.5Nb	450	500	100
iHEA-1Nb	450	500	100

[1] Certain commercial equipment, instruments, open-source software, or materials are identified in this paper to foster understanding. Such identification does not imply recommendation or endorsement by the National Institute of Standards and Technology, nor does it imply that the materials or equipment identified are necessarily the best available for the purpose.

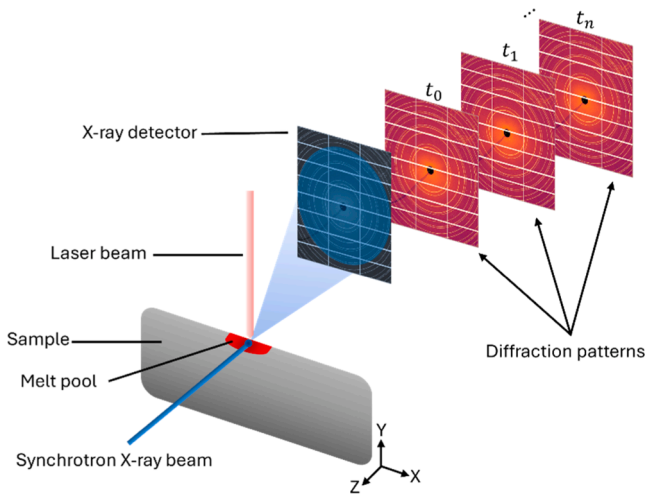

Fig. 1. Schematic representation of an in-situ laser-melting X-ray diffraction experiment, t_0 is related to the initial time for the experiment.

SXRD patterns acquired before and after laser melting for the iHEAs. It is acknowledged that the Scheil-Gulliver model is based on three key assumptions: (1) no back diffusion occurs in the solid phase; (2) diffusion in the liquid phase is sufficiently fast to maintain a homogeneous composition; and (3) local equilibrium is maintained at the solid-liquid interface [27]. While the Scheil model offers insight into potential solidification trends, it may not fully reflect the rapid solidification conditions in AM. Phases like NbC may form via solid-state transformations; therefore, the results are interpreted qualitatively to provide insight into the phase evolution. In Fig. 2a, the alloy without Nb additions (iHEA) is predicted to form a Cr-rich (σ) phase (e.g., (Fe, Mn)Cr-type intermetallic), followed by the stabilization of the γ-f.c.c. matrix. In contrast, for the Nb-containing alloys, the formation of NbC is also predicted alongside σ and γ-f.c.c. phases. A magnified view of the region corresponding to the formation of NbC carbides in iHEA-0.5Nb and iHEA-1Nb alloys is shown in Fig. 2b The SXRD patterns (Fig. 2c) provide experimental validation of the phase evolution. In the as-fabricated state, the iHEA without Nb shows a single γ-f.c.c. phase, with a minor fraction of ε-h.c.p. phase. Upon the Nb addition, both iHEA-0.5Nb and iHEA-1Nb exhibit the formation of NbC carbides, with no detectable σ phase in any condition. Notably, the iHEA-0.5Nb alloy shows a negligible amount of NbC before laser melting, with a phase fraction of <0.05. The Williamson-Hall equation [28] applied to the iHEAs after laser melting reveals a transition from a coarse-grained microstructure in the Nb-free alloy (66.7 nm crystallite size, 2.25 × 10^{14} m^{-2} dislocation density) to a more refined state with 0.5Nb addition (41.8 nm crystallite size, 5.72 × 10^{14} m^{-2} dislocation density), suggesting Nb-driven heterogeneous nucleation and an increased dislocation density. However, increasing the Nb content to 1Nb results in moderate crystallite growth (51.8 nm, 3.73 × 10^{14} m^{-2} dislocation density), indicating a competition between refinement and coarsening mechanisms. According to Zhang et al. [14], the increased dislocation density in the iHEA-Nb samples is primarily attributed to the obstruction of dislocation motion by Nb-containing particles, which causes entanglement and accumulation, as well as the thermal expansion mismatch between these particles and the FCC matrix, leading to additional dislocations. These results suggest that while Nb initially aids in dislocation generation and crystallite refinement,

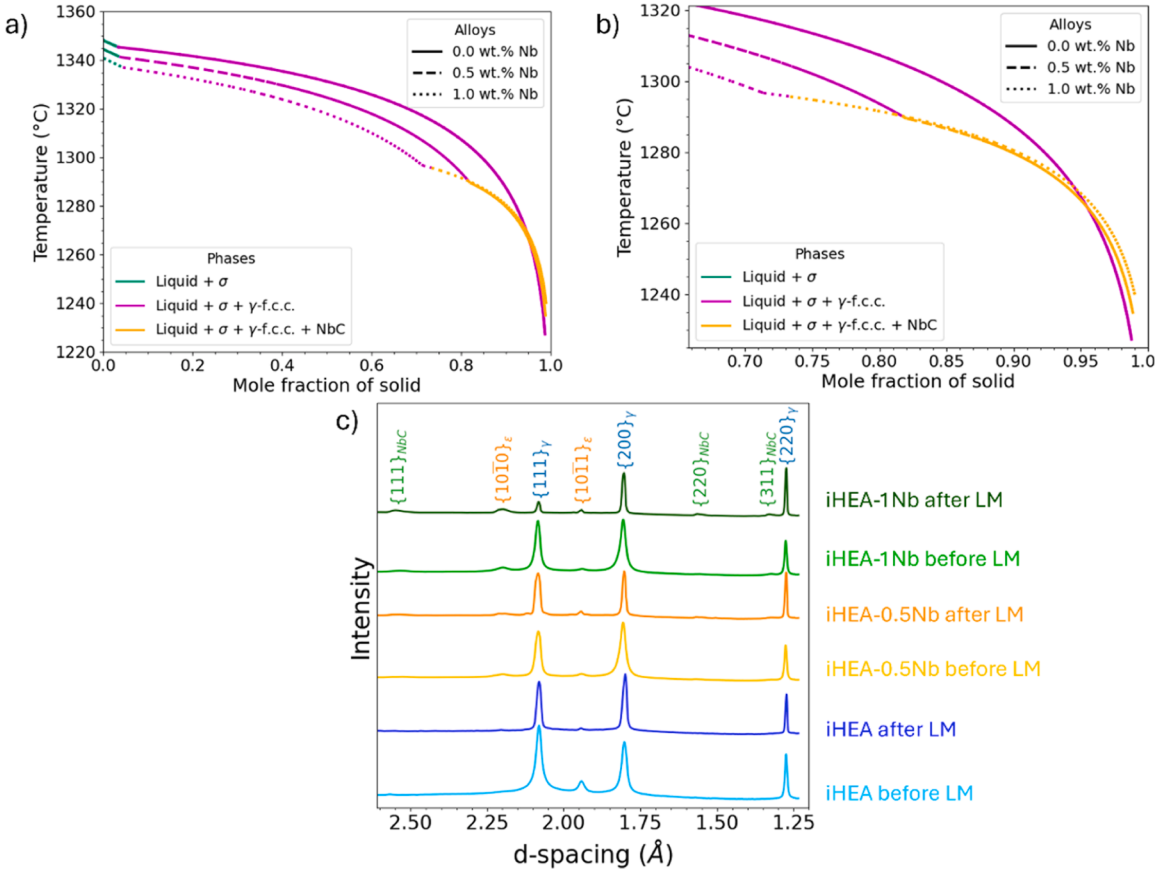

Fig. 2. a) Scheil-Gulliver solidification curves for the iHEAs, b) Magnified view highlighting the NbC formation region, c) SXRD before and after laser-melting for iHEAs. Both γ-f.c.c. and NbC phases crystallize in the Fm$\bar{3}$m space group. The lattice parameters for the γ-f.c.c. are 3.604 Å, 3.608 Å, 3.612 Å for iHEA, iHEA-0.5Nb, and iHEA-1Nb, respectively, while the NbC lattice parameters are 4.397 Å and 4.412Å for iHEA-0.5Nb and iHEA-1Nb, respectively.

excessive Nb content may reduce its effectiveness due to solubility limits and the precipitation of secondary phases. This behavior aligns with previous findings suggesting that beyond critical concentration, Nb ceases to significantly refine crystallite size once its role in nucleation is exhausted, or it remains in solid solution [29].

3.2. Real-time phase evolution during solidification

Fig. 3 presents the integrated SXRD pattern evolution during solidification for all three studied iHEAs. Fig. 3(d,e) shows the volumetric phase fraction evolution as a function of time for the Nb-containing alloys. Since the Nb-free iHEA displayed only minimal ε-h.c.p. content (as seen in Fig. 2c and Fig. 3a), the phase fraction analysis was concentrated on the 0.5Nb and 1Nb compositions. The results reveal a strong compositional dependence on phase selection in the studied iHEA compositional system. At the onset of the experiment, before the laser interacts with the SXRD-monitored volume, the iHEA (Fig. 3a) exhibited a dominant γ-f.c.c. phase, accompanied by low-intensity ε-h.c.

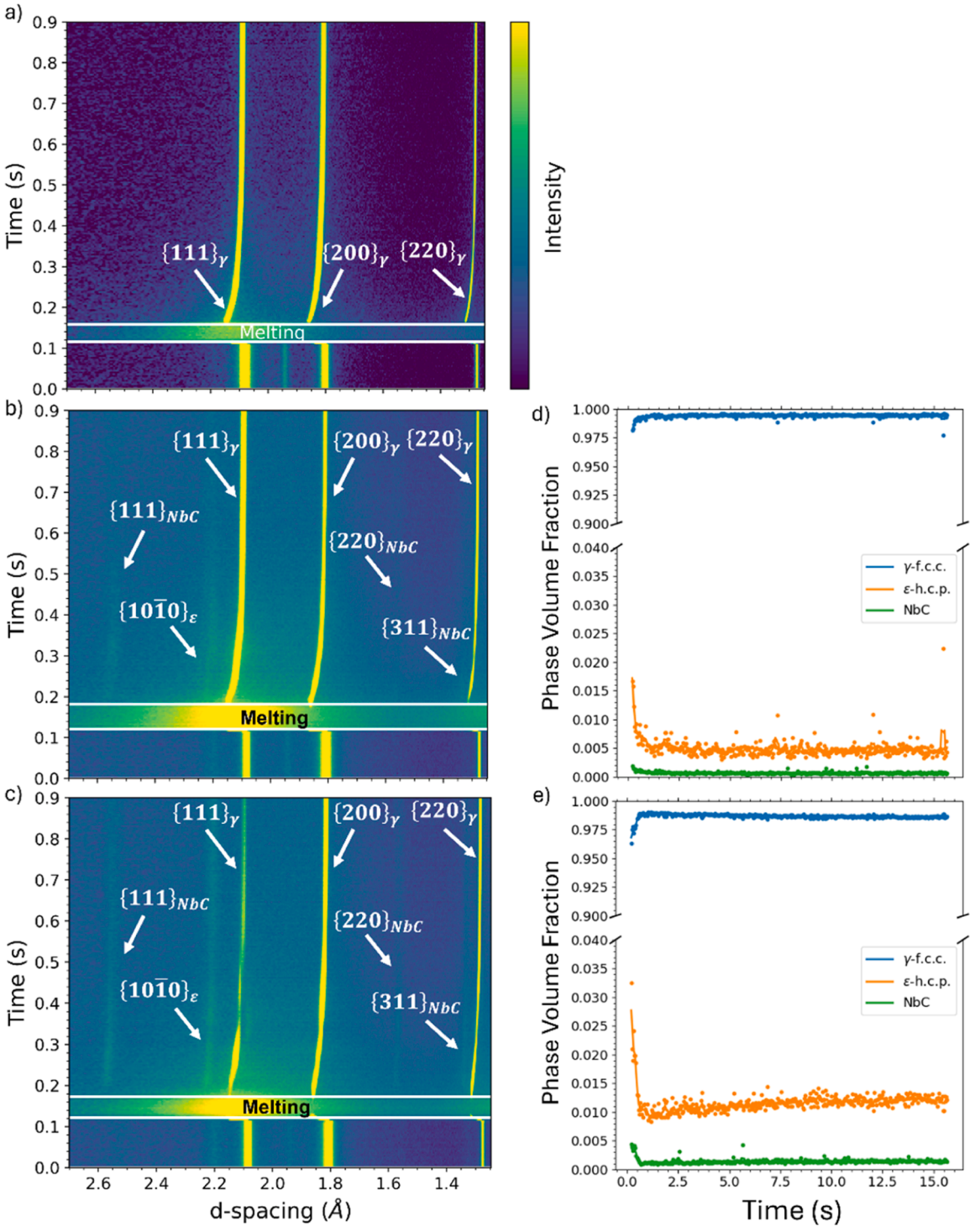

Fig. 3. SXRD intensity map during laser melting of a) iHEA Nb free; b) iHEA-0.5Nb; and c) iHEA-1Nb. Evolution of phase volume fractions for (d) iHEA-0.5Nb and (e) iHEA-1Nb experiments. The time zero for phase fraction quantification corresponds to the onset of sample solidification.

p. reflections, consistent with the equilibrium microstructure previously shown in Fig. 2c. Melting of the analyzed material occurs in ≈ 150 ms, after which diffraction peaks reappear corresponding to γ-f.c.c., ε-h.c.p., and NbC phases (with a melting point estimated via CALPHAD-based thermodynamic calculations [30] to be 1323.9 °C). These peaks progressively shift toward higher diffraction angles due to thermal contraction during cooling.

While the iHEA resolidifies as a single γ-f.c.c. phase, both iHEA-0.5Nb and iHEA-1Nb present a multiphase microstructure development, consisting of γ-f.c.c., ε-h.c.p., and NbC phases. Notably, the commonly observed Laves and σ phases in Nb-containing HEAs [15,31] are absent in all conditions, suggesting a unique kinetic pathway under rapid solidification conditions. Increasing the Nb content from 0.5Nb to 1Nb leads to a noticeable reduction in the $\{111\}_{\gamma}$ peak intensity, while the NbC and ε-h.c.p. diffraction signals strengthen (Fig. 3(b,c)). This trend aligns with previous studies on AlCrFeCoNiNb HEAs, where Nb addition suppresses γ-f.c.c. phase formation [15]. Furthermore, NbC formation is favored due to the rapid cooling kinetics and the strong affinity between Nb and C [14,32] which promotes its preferential nucleation.

In-situ SXRD suggests NbC precipitation may occur dynamically during solidification, as indicated by the emergence of NbC peaks with significant intensity, which are absent in the iHEAs before laser melting (Fig. 2c). The delayed appearance of NbC relative to the γ-f.c.c. phase (Fig. 3(b,c)) implies a diffusion-controlled growth mechanism, consistent with the need for Nb and C partitioning and solute redistribution during cooling [33], as well as with the sluggish diffusion kinetics typical of HEAs [34,35].

A further effect of Nb alloying is the progressive increase in the ε-h.c.p. phase fraction, suggesting a systematic reduction in stacking fault energy (SFE) of the γ-f.c.c. matrix, aligning with findings in Nb-containing austenitic steels, where Nb lowers SFE by modifying the electronic structure (i.e., electron-to-atom ratio) [36]. Metastable γ-f.c.c. structures facilitate deformation-induced phase transformations due to their typically low SFE [10,37,38], which is further reduced by γ-f.c.c. carbon depletion owing to NbC precipitation. Since carbon stabilizes the γ-f.c.c. phase by increasing SFE, its removal from the γ-f.c.c. matrix enhances the γ-f.c.c.→ε-h.c.p. transformation [39–41]. This coupling of Nb-driven carbon depletion and direct SFE manipulation results in a synergistic promotion of ε-h.c.p. formation. Wang et al. [42] have reported a similar phenomenon in a $Fe_{49}Mn_{30}Co_{10}Cr_{10}C_{1.0}$ (at. %) iHEA, where Nb addition led to a measurable decrease in SFE and an increase in the ε-h.c.p. phase volume fraction, corroborating our findings.

3.3. Lattice parameter evolution and structural anisotropy

Fig. 4 illustrates the evolution of the γ-f.c.c. lattice parameter calculated from multiple crystallographic reflections, offering insight into both the structural evolution and anisotropy behavior of the phase during solidification. A more detailed analysis of γ-f.c.c. lattice anisotropy can be found in [43]. As shown in Figs. 4a–c, all investigated iHEAs exhibit an initial rapid contraction of the lattice parameter due to thermal shrinkage upon cooling. However, with increasing Nb content, this contraction rate decreases progressively, indicating that Nb modifies the thermal response of the lattice. Additionally, Nb addition led to a higher final γ-f.c.c. lattice parameter after solidification (Fig. 4d), consistent with earlier findings by Cheng et al. [17], who attributed similar behavior in Nb-alloyed CoCrCuFeNi HEAs to lattice expansion effects from the larger atomic radius of Nb. This increase in lattice parameter is likely the result of cumulative strain induced by atomic size mismatch [15,16], combined with residual thermal stresses from the high thermal gradients and rapid solidification rates characteristic of

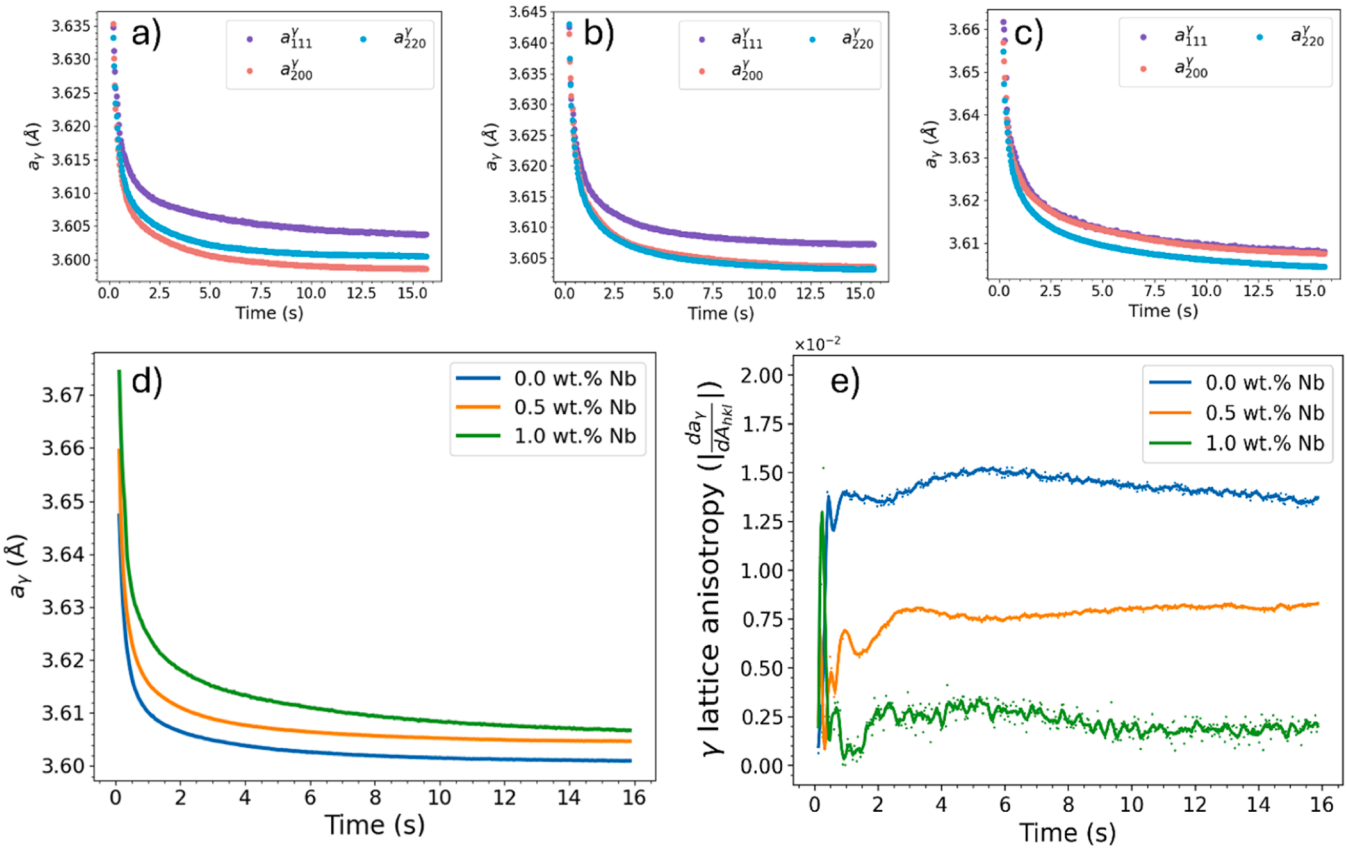

Fig. 4. Lattice parameter variation during cooling for a) iHEA, b) iHEA-0.5Nb, c) iHEA-1Nb, d) Average lattice parameter for the iHEAs, and e) Lattice anisotropy for the FCC phase for the three alloys. Only cooling after melting was considered. The time zero corresponds to the onset of the sample solidification.

laser melting (10^5–10^6 K/s) [44,45]. These strain effects influence not only the lattice spacing but also phase stability and elastic deformation, as captured during in situ SXRD.

Beyond altering the lattice parameter, Nb incorporation also influences the microstructural evolution by forming NbC and ε-h.c.p. phases, as shown in Fig. 2c, Fig. 3d, and Fig. 3e. These secondary phases act as barriers to grain growth and mobility, disrupting preferred crystallographic orientations and resulting in a more heterogeneous microstructure. Interestingly, while Tian et al. [46] reported that incorporating an element with a larger atomic radius enhances anisotropy, our findings reveal the opposite trend: Nb addition reduces lattice anisotropy (Fig. 4e). This behavior may be rationalized by considering the electronic structure of HEAs. Yen et al. [47] investigated the influence of lattice distortion on HEA anisotropy and observed that, in systems with significant atomic size differences but similar bond strengths, structural distortion increases anisotropy, provided electron density inconsistency is minimal. However, in HEAs, electron density inconsistency appears to play a more dominant role than atomic size differences. In this context, we propose that the observed reduction in anisotropy with Nb addition primarily stems from modifications in electron density distribution, which counterbalance the effects of increased lattice distortion. This suggests that rather than amplifying anisotropy as in dilute solid solutions [47], severe lattice distortions in these iHEAs may suppress preferential grain orientation, enhance defect interactions, and modify deformation mechanisms, ultimately promoting a more isotropic elastic response.

3.4. Crystallographic orientation evolution during solidification

To further investigate these effects, Fig. 5 illustrates the evolution of γ-f.c.c. peak relative intensities during cooling, revealing distinct Nb-driven solidification pathways. The calculated γ-f.c.c. relative peak intensities for an ideal random polycrystal are represented by dotted lines, with the corresponding family plane labeled on the right side of each panel. In the iHEA (Fig. 5a), the $\{200\}_\gamma$ peak emerges as the most intense, while the $\{111\}_\gamma$ peak intensity decreased concurrently. The $\{220\}_\gamma$ peak displayed the lowest intensity throughout cooling. Incorporating 0.5Nb (Fig. 5b) alters this behavior. The $\{200\}_\gamma$ peak intensity increase is delayed, showing two rapid growth intervals. Meanwhile, the $\{111\}_\gamma$ peak intensity, after an initial decrease, recovers significantly, reaching nearly 90 % of its calculated value. The inversion of intensity dominance between the $\{111\}_\gamma$ and $\{200\}_\gamma$ peaks resembles the behavior in the Nb-free alloy. Interestingly, the substantial initial intensity increase of $\{220\}_\gamma$ peak suggests grain orientation competition and Nb-induced preferred orientation modifications. These peak intensity oscillations are consistent with the preferential segregation model proposed by Luo [48], wherein Nb atoms selectively segregate to specific grain boundaries or crystallographic planes. This segregation alters the local free energy landscape during solidification, dynamically driving orientation rearrangements.

Furthermore, the suppression of the $\{111\}_\gamma$ peak intensity, along with the concurrent increase in the $\{220\}_\gamma$ peak intensity with 1Nb addition (Fig. 5c), reflects a significant shift in the crystallographic orientation landscape, attributed to multiple synergistic mechanisms. First, the expansion of the γ-f.c.c. lattice parameter due to Nb incorporation (Fig. 4a-d) introduces distortions that disrupt the preferred crystallographic orientation, leading to a more randomized grain distribution. Second, the concurrent formation of NbC and ε-h.c.p. phases, observed in Fig. 2 and Fig. 3, hinders grain growth and modifies preferred orientation development by acting as physical barriers. Third, a potential reduction in SFE with Nb addition may enhance defect formation, including dislocations and twins, further disrupting orientation uniformity. Consequently, the significant decrease in $\{111\}_\gamma$ peak

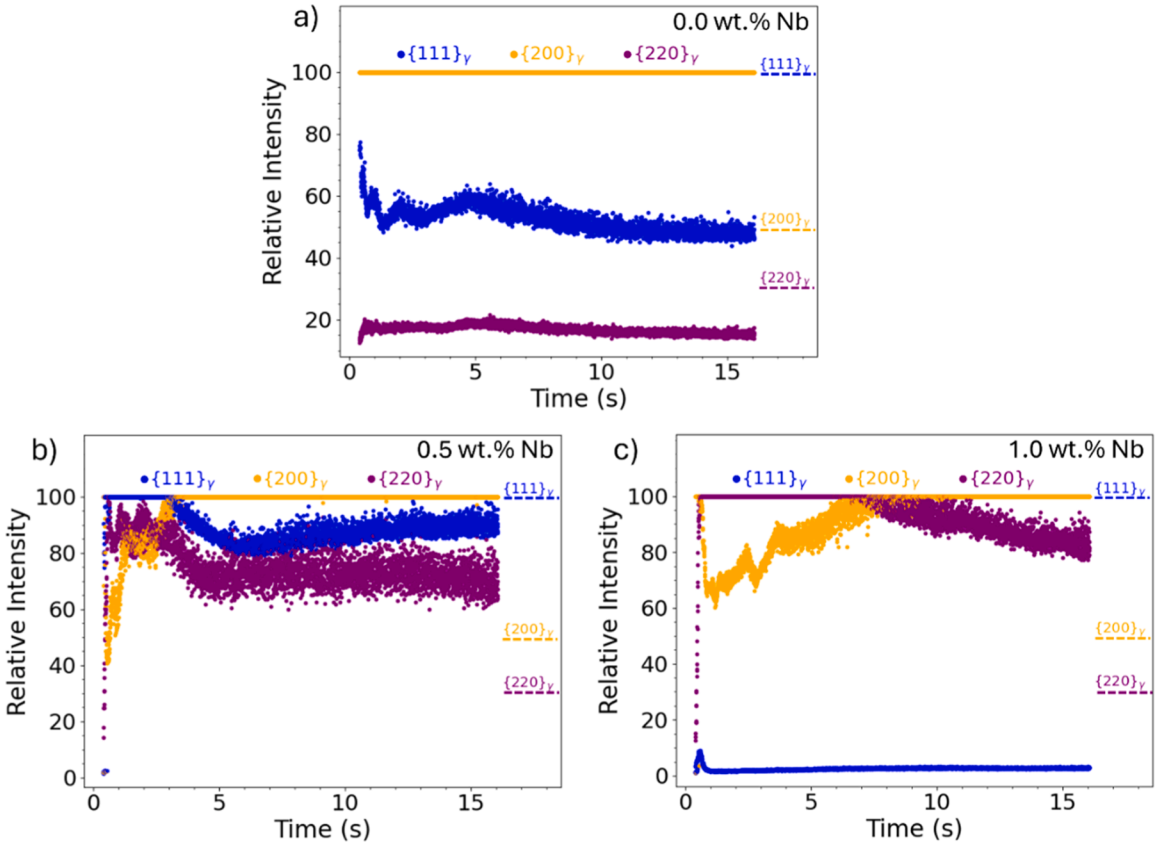

Fig. 5. SXRD relative intensity of the γ-f.c.c. peaks during the cooling from the liquid phase of a) iHEA, b) iHEA-0.5Nb, and c) iHEA-1Nb.

intensity, coupled with the pronounced increase in $\{220\}_{\gamma}$ peak intensity demonstrates changes in crystallographic orientation, indicating a shift away from preferential grain alignment.

3.5. Implications of Nb-induced microstructural engineering

The comprehensive in situ analysis presented here underscores how Nb incorporation fundamentally reshapes the microstructural evolution pathways of FeMnCoCrC iHEAs during rapid solidification. From promoting NbC precipitation and ε-h.c.p. phase formation to modulating lattice anisotropy and crystallographic orientation, Nb acts as an alloying addition and as a key microstructural tuning agent. These transformations highlight the critical sensitivity of iHEAs to compositional tailoring under non-equilibrium processing conditions. The findings also reveal how subtle adjustments in alloy chemistry can result in non-trivial changes in defect structures, phase balance, and crystallographic orientation. This positions Nb as a strategic lever for designing next-generation high-performance alloys optimized for advanced manufacturing techniques.

4. Conclusions

This study investigated the effects of Nb addition on the microstructural evolution and phase stability of FeMnCoCrC iHEAs under rapid solidification conditions via in situ synchrotron X-ray diffraction during laser melting. The main conclusions are as follows:

1. Nb promotes heterogeneous nucleation, leading to significant crystallite refinement and increased dislocation density at lower concentrations. However, a saturation effect is observed at higher Nb content, where partial coarsening and dislocation density reduction occur, suggesting a competing interplay between refinement mechanisms and phase stability.
2. The introduction of Nb suppresses the formation of the σ phase and instead favors the precipitation of NbC and ε-h.c.p. phases. These phase transformations are strongly influenced by NbC interactions and the rapid cooling rates characteristic of laser melting.
3. Nb induces lattice expansion due to atomic size mismatch, contributing to structural distortion. Despite expectations, Nb reduces γ-f.c.c. lattice anisotropy, likely due to changes in electron density distribution, indicating a complex interplay between atomic structure and electronic effects in iHEAs.
4. The shift in γ-f.c.c. peak intensities, particularly the suppression of $\{111\}_{\gamma}$ and enhancement of $\{220\}_{\gamma}$ peaks, reflect a disruption of preferential grain alignment, reinforcing the role of Nb in modifying grain orientation and overall phase stability.
5. Nb-driven NbC precipitation depletes carbon from the matrix, reducing SFE and enhancing the formation of ε-h.c.p. phase. This mechanism is central to the observed increase in microstructural heterogeneity and crystallographic structure evolution during solidification.

Overall, this work reveals the critical role of Nb in tailoring the microstructure of FeMnCoCrC iHEAs through a combination of lattice distortion, phase selection, and crystallographic structure control. These mechanisms are especially relevant under rapid solidification conditions, such as those encountered in laser-based additive manufacturing. The findings pave the way for the strategic design of Nb-containing iHEAs with enhanced mechanical performance, particularly for applications requiring high microstructural stability and tunable deformation behavior. Future studies should expand on these results by correlating the observed microstructural phenomena with mechanical testing and long-term performance under service-relevant conditions.

CRediT authorship contribution statement

I.A.B. Moura: Writing – review & editing, Writing – original draft, Visualization, Validation, Methodology, Investigation, Formal analysis, Data curation, Conceptualization. **G.G. Ribamar:** Writing – review & editing, Visualization, Validation, Software, Investigation, Formal analysis, Data curation. **A.C. Chuang:** Writing – original draft, Visualization, Validation, Investigation, Data curation. **T.S. Nunes:** Writing – review & editing, Visualization, Validation, Investigation. **Jiajia Shen:** Writing – review & editing, Visualization, Validation, Investigation. **Wei Zhang:** Writing – review & editing, Visualization, Validation, Methodology, Investigation. **P. Freitas Rodrigues:** Writing – review & editing, Visualization, Validation. **A.B. Pereira:** Writing – review & editing, Visualization, Validation. **Yutao Pei:** Visualization, Validation, Investigation. **F. Zhang:** Writing – review & editing, Visualization, Validation, Resources, Methodology, Data curation. **J.P. Oliveira:** Writing – review & editing, Visualization, Validation, Supervision, Resources, Project administration, Methodology, Investigation, Funding acquisition, Conceptualization.

Declaration of competing interest

The authors declare that they have no known competing financial interests or personal relationships that could have appeared to influence the work reported in this paper.

Acknowledgments

I. A. B. Moura acknowledges Fundação para a Ciência e Tecnologia (FCT – MCTES) for funding the PhD grant (2021.08034.BD). JS and JPO acknowledge the funding by national funds from FCT - Fundação para a Ciência e a Tecnologia, I.P., in the scope of the project's LA/P/0037/2020, UIDP/50025/2020 and UIDB/50025/2020 of the Associate Laboratory Institute of Nanostructures, Nanomodelling and Nanofabrication – i3N. P.F.R. acknowledges funding by FCT – Fundação para a Ciência e a Tecnologia, under projects UID/00285 - Centre for Mechanical Engineering, Materials and Processes, LA/P/0112/2020 and CAPES - Novação - 99999.011943/2013–00. This research used resources of the Advanced Photon Source, a U.S. Department of Energy (DOE) Office of Science user facility operated for the DOE Office of Science by Argonne National Laboratory under Contract No. DE-AC02–06CH11357. The present study was developed in the scope of the Project "Agenda ILLIANCE" [C644919832–00000035 | Project n° 46], financed by PRR – Plano de Recuperação e Resiliência under the Next Generation EU from the European Union.

References

[1] M. Wang, Y. Lu, T. Wang, C. Zhang, Z. Cao, T. Li, P.K. Liaw, A novel bulk eutectic high-entropy alloy with outstanding as-cast specific yield strengths at elevated temperatures, Scr. Mater. 204 (2021) 114132, https://doi.org/10.1016/j.scriptamat.2021.114132.

[2] Y.L. Zhao, T. Yang, J.H. Zhu, D. Chen, Y. Yang, A. Hu, C.T. Liu, J.-J. Kai, Development of high-strength Co-free high-entropy alloys hardened by nanosized precipitates, Scr. Mater. 148 (2018) 51–55, https://doi.org/10.1016/j.scriptamat.2018.01.028.

[3] T. Yang, Y.L. Zhao, J.H. Luan, B. Han, J. Wei, J.J. Kai, C.T. Liu, Nanoparticles-strengthened high-entropy alloys for cryogenic applications showing an exceptional strength-ductility synergy, Scr. Mater. 164 (2019) 30–35, https://doi.org/10.1016/j.scriptamat.2019.01.034.

[4] R.S. Mishra, R.S. Haridas, P. Agrawal, High entropy alloys – Tunability of deformation mechanisms through integration of compositional and microstructural domains, Mater. Sci. Eng. A 812 (2021) 141085, https://doi.org/10.1016/j.msea.2021.141085.

[5] M.R. Barnett, M. Senadeera, D. Fabijanic, K.F. Shamlaye, J. Joseph, S.R. Kada, S. Rana, S. Gupta, S. Venkatesh, A scrap-tolerant alloying concept based on high entropy alloys, Acta Mater. 200 (2020) 735–744, https://doi.org/10.1016/j.actamat.2020.09.027.

[6] P. Chen, S. Li, Y. Zhou, M. Yan, M.M. Attallah, Fabricating CoCrFeMnNi high entropy alloy via selective laser melting in-situ alloying, J. Mater. Sci. Technol. 43 (2020) 40–43, https://doi.org/10.1016/j.jmst.2020.01.002.

[7] M. Wang, Z. Li, D. Raabe, In-situ SEM observation of phase transformation and twinning mechanisms in an interstitial high-entropy alloy, Acta Mater. 147 (2018) 236–246, https://doi.org/10.1016/j.actamat.2018.01.036.

[8] Z. Li, C.C. Tasan, H. Springer, B. Gault, D. Raabe, Interstitial atoms enable joint twinning and transformation induced plasticity in strong and ductile high-entropy alloys, Sci. Rep. 7 (2017) 40704, https://doi.org/10.1038/srep40704.

[9] Q. Yu, S. Qiu, Z.-B. Jiao, Atomic-scale understanding of interstitial-strengthened high-entropy alloys, Rare Metals. (2025), https://doi.org/10.1007/s12598-025-03358-z.

[10] W. Zhang, H. Wang, B.J. Kooi, Y. Pei, Additive manufacturing of interstitial-strengthened high entropy alloy: scanning strategy dependent anisotropic mechanical properties, Mater. Sci. Eng. A 872 (2023) 144978, https://doi.org/10.1016/j.msea.2023.144978.

[11] W. Zhang, J. Shen, J.P. Oliveira, B.J. Kooi, Y. Pei, Crystallographic orientation-dependent deformation characteristics of additive manufactured interstitial-strengthened high entropy alloys, Scr. Mater. 222 (2023) 115049, https://doi.org/10.1016/j.scriptamat.2022.115049.

[12] W. Zhang, J. Shen, J.P. Oliveira, H. Wang, S. Feng, N. Schell, B.J. Kooi, Y. Pei, Deformation processes of additively manufactured interstitial-strengthened high entropy alloy: in-situ high-energy synchrotron X-ray diffraction and microstructural appraisal, Addit. Manuf. 76 (2023) 103791, https://doi.org/10.1016/j.addma.2023.103791.

[13] A. Chabok, W. Zhang, J. Shen, J.P. Oliveira, H. Wang, S. Feng, N. Schell, B.J. Kooi, Y. Pei, On the orientation-dependent mechanical properties of interstitial solute-strengthened Fe49.5Mn30Co10Cr10C0.5 high entropy alloy produced by directed energy deposition, Addit. Manuf. 79 (2024) 103914, https://doi.org/10.1016/j.addma.2023.103914.

[14] W. Zhang, A. Chabok, H. Wang, J. Shen, J.P. Oliveira, S. Feng, N. Schell, B.J. Kooi, Y. Pei, Ultra-strong and ductile precipitation-strengthened high entropy alloy with 0.5 % Nb addition produced by laser additive manufacturing, J. Mater. Sci. Technol. 187 (2024) 195–211, https://doi.org/10.1016/j.jmst.2023.11.053.

[15] W.H. Liu, J.Y. He, H.L. Huang, H. Wang, Z.P. Lu, C.T. Liu, Effects of Nb additions on the microstructure and mechanical property of CoCrFeNi high-entropy alloys, Intermetallics 60 (2015) 1–8, https://doi.org/10.1016/j.intermet.2015.01.004.

[16] R. Li, J. Ren, G.-J. Zhang, J.-Y. He, Y.-P. Lu, T.-M. Wang, T.-J. Li, Novel (CoFe2NiV0.5Mo0.2)100−xNbx eutectic high-entropy alloys with excellent combination of mechanical and corrosion properties, Acta Metallurgica Sinica 33 (2020) 1046–1056, https://doi.org/10.1007/s40195-020-01072-6.

[17] J.B. Cheng, X.B. Liang, B.S. Xu, Effect of Nb addition on the structure and mechanical behaviors of CoCrCuFeNi high-entropy alloy coatings, Surf. Coat. Technol. 240 (2014) 184–190, https://doi.org/10.1016/j.surfcoat.2013.12.053.

[18] X. Ji, K. Guan, Y. Bao, Z. Mao, F. Wang, H. Dai, Effect of Nb addition on the corrosion and wear resistance of laser clad AlCr2FeCoNi high-entropy alloy coatings, Lubricants. 12 (2024), https://doi.org/10.3390/lubricants12010005.

[19] S.A. Oh, R.E. Lim, J.W. Aroh, A.C. Chuang, B.J. Gould, J.V. Bernier, N. Parab, T. Sun, R.M. Suter, A.D. Rollett, Microscale observation via high-speed X-ray diffraction of alloy 718 during In situ laser melting, JOM 73 (2021) 212–222, https://doi.org/10.1007/s11837-020-04481-1.

[20] Z. Zhang, X. Li, H. Yi, H. Xie, Z. Zhao, P. Bai, Clarify the role of Nb alloying on passive film and corrosion behavior of CoCrFeMnNi high entropy alloy fabricated by laser powder bed fusion, Corros. Sci. 224 (2023) 111510, https://doi.org/10.1016/j.corsci.2023.111510.

[21] J.W. Pegues, M.A. Melia, S.R. Whetten, M.A. Rodriguez, E.J. Barrick, N. Argibay, A. B. Kustas, Accelerated screening of tax(CoCrFeMnNi)1-x and nbx(CoCrFeMnNi)1-x high-entropy alloys, J. Mater. Process. Technol. 319 (2023) 118017, https://doi.org/10.1016/j.jmatprotec.2023.118017.

[22] J. Xu, R. Duan, K. Feng, C. Zhang, Q. Zhou, P. Liu, Z. Li, Enhanced strength and ductility of laser powder bed fused NbMoTaW refractory high-entropy alloy via carbon microalloying, Addit. Manuf. Lett. 3 (2022), https://doi.org/10.1016/j.addlet.2022.100079.

[23] M. Storm, G. Lotze, pydidas - Python Diffraction Data Analysis Suite (v24.09.19), (2024).

[24] B. Cullity, Elements of X-ray Diffraction, ADDISONWESLEY PUBLISHING COMPANY, INC., READING, MASSACHUSETTS, 1956.

[25] G.A. Faria, Exploring Metallic Materials Behavior Through in Situ Crystallographic Studies By Synchrotron Radiation, Universidade Estadual de Campinas, 2014, https://doi.org/10.47749/T/UNICAMP.2014.942993.

[26] J.D. Escobar, G.A. Faria, L. Wu, J.P. Oliveira, P.R. Mei, A.J. Ramirez, Austenite reversion kinetics and stability during tempering of a Ti-stabilized supermartensitic stainless steel: correlative in situ synchrotron x-ray diffraction and dilatometry, Acta Mater. 138 (2017) 92–99, https://doi.org/10.1016/j.actamat.2017.07.036.

[27] D. Durinck, P.T. Jones, B. Blanpain, P. Wollants, G. Mertens, J. Elsen, Slag solidification modeling using the Scheil–Gulliver assumptions, J. Am. Ceramic Soc. 90 (2007) 1177–1185, https://doi.org/10.1111/j.1551-2916.2007.01597.x.

[28] G.K. Williamson, W.H. Hall, X-ray line broadening from filed aluminium and wolfram, Acta Metallurgica 1 (1953) 22–31, https://doi.org/10.1016/0001-6160(53)90006-6.

[29] S. Mula, H. Bahmanpour, S. Mal, P.C. Kang, M. Atwater, W. Jian, R.O. Scattergood, C.C. Koch, Thermodynamic feasibility of solid solubility extension of Nb in Cu and their thermal stability, Mater. Sci. Eng. A 539 (2012) 330–336, https://doi.org/10.1016/j.msea.2012.01.104.

[30] N. Saunders, A.P. Miodownik, CALPHAD (calculation of Phase diagrams): a Comprehensive Guide, 1st ed., Pergamon Press, Oxford, 1998.

[31] S.G. Ma, Y. Zhang, Effect of Nb addition on the microstructure and properties of AlCoCrFeNi high-entropy alloy, Mater. Sci. Eng. A 532 (2012) 480–486, https://doi.org/10.1016/j.msea.2011.10.110.

[32] Y. Bai, D. Jiao, J. Li, Z. Yang, Effect of Nb content on the stacking fault energy, microstructure and mechanical properties of Fe-25Mn-9Al-8Ni-1C alloy, Mater. Today Commun. 31 (2022) 103554, https://doi.org/10.1016/j.mtcomm.2022.103554.

[33] J.N. Dupont, C.V. Robino, B.D. Newbury, Modeling solute redistribution and microstructural development in fusion welds of multi-component alloys, 1999.

[34] J.W. Yeh, Recent progress in high-entropy alloys, Annales de Chimie: Science Des Materiaux 31 (2006) 633–648, https://doi.org/10.3166/acsm.31.633-648.

[35] E.P. George, W.A. Curtin, C.C. Tasan, High entropy alloys: a focused review of mechanical properties and deformation mechanisms, Acta Mater. 188 (2020) 435–474, https://doi.org/10.1016/j.actamat.2019.12.015.

[36] L.G. Martinez, K. Imakuma, A.F. Padilha, Influence of niobium on stacking-fault energy of all-austenite stainless steels, Steel Res. 63 (1992) 221–223, https://doi.org/10.1002/srin.199200503.

[37] S. Allain, J.P. Chateau, O. Bouaziz, S. Migot, N. Guelton, Correlations between the calculated stacking fault energy and the plasticity mechanisms in Fe-Mn-C alloys, Mater. Sci. Eng. A 387–389 (2004) 158–162, https://doi.org/10.1016/j.msea.2004.01.059.

[38] I.A.B. Moura, G.G. Ribamar, P. Agrawal, A. Roy, J. Shen, P.F. Rodrigues, E. Maawad, N. Schell, A.B. Pereira, J.P. Oliveira, R.S. Mishra, Influence of B4C alloying on the phase stability of Fe-Mn-Co-Cr-Si high entropy alloys fabricated using laser powder bed fusion, Mater. Sci. Eng. A (2025) 148607, https://doi.org/10.1016/j.msea.2025.148607.

[39] A. Abbasi, A. Dick, T. Hickel, J. Neugebauer, First-principles investigation of the effect of carbon on the stacking fault energy of Fe–C alloys, Acta Mater. 59 (2011) 3041–3048, https://doi.org/10.1016/j.actamat.2011.01.044.

[40] A. Saeed-Akbari, J. Imlau, U. Prahl, W. Bleck, Derivation and variation in composition-dependent stacking fault energy maps based on subregular solution model in high-manganese steels, Metall. Mater. Trans. A 40 (2009) 3076–3090, https://doi.org/10.1007/s11661-009-0050-8.

[41] M. Frank, Y. Chen, S.S. Nene, S. Sinha, K. Liu, K. An, R.S. Mishra, Investigating the deformation mechanisms of a highly metastable high entropy alloy using in-situ neutron diffraction, Mater. Today Commun. 23 (2020) 100858, https://doi.org/10.1016/j.mtcomm.2019.100858.

[42] Q. Wang, Y. Zhou, X. Deng, Z. Wang, Achieving excellent mechanical properties and wear resistance in Fe49Mn30Co10Cr10C1 interstitial high-entropy alloy via tuning composition and stacking fault energy by Nb doping, Wear 534–535 (2023) 205149, https://doi.org/10.1016/j.wear.2023.205149.

[43] G.G. Ribamar, G. Miyamoto, T. Furuhara, J.D. Escobar, J.A. Ávila, E. Maawad, N. Schell, J.P. Oliveira, H. Goldenstein, On the evolution of austenite during tempering in high-carbon high-silicon bearing steel by high energy X-ray diffraction, Metall. Mater. Trans. A 55 (2024) 93–100, https://doi.org/10.1007/s11661-023-07229-z.

[44] Z. Tong, X. Ren, J. Jiao, W. Zhou, Y. Ren, Y. Ye, E.A. Larson, J. Gu, Laser additive manufacturing of FeCrCoMnNi high-entropy alloy: effect of heat treatment on microstructure, residual stress and mechanical property, J. Alloys. Compd. 785 (2019) 1144–1159, https://doi.org/10.1016/j.jallcom.2019.01.213.

[45] F. Liu, X. Lin, G. Yang, M. Song, J. Chen, W. Huang, Microstructure and residual stress of laser rapid formed Inconel 718 nickel-base superalloy, Opt. Laser. Technol. 43 (2011) 208–213, https://doi.org/10.1016/j.optlastec.2010.06.015.

[46] F. Tian, L.K. Varga, N. Chen, L. Delczeg, L. Vitos, *Ab initio* investigation of high-entropy alloys of 3 <math display="inline"><mi>d</mi></math>elements, Phys. Rev. B 87 (2013) 075144, https://doi.org/10.1103/PhysRevB.87.075144.

[47] C.-C. Yen, G.-R. Huang, Y.-C. Tan, H.-W. Yeh, D.-J. Luo, K.-T. Hsieh, E.-W. Huang, J.-W. Yeh, S.-J. Lin, C.-C. Wang, C.-L. Kuo, S.-Y. Chang, Y.-C. Lo, Lattice distortion effect on elastic anisotropy of high entropy alloys, J. Alloys. Compd. 818 (2020) 152876, https://doi.org/10.1016/j.jallcom.2019.152876.

[48] J. Luo, Grain boundary segregation models for high-entropy alloys: theoretical formulation and application to elucidate high-entropy grain boundaries, J. Appl. Phys. 135 (2024), https://doi.org/10.1063/5.0200669.